



**HAL**  
open science

## Ar(1s<sub>5</sub>) density in a co-axial argon plasma jet with N<sub>2</sub>-O<sub>2</sub> shielding

Duarte Gonçalves, Gérard Bauville, Pascal Jeanney, Mario Lino da Silva, Luis Lemos Alves, Stéphane Pasquiers, Joao Santos Sousa

► **To cite this version:**

Duarte Gonçalves, Gérard Bauville, Pascal Jeanney, Mario Lino da Silva, Luis Lemos Alves, et al.. Ar(1s<sub>5</sub>) density in a co-axial argon plasma jet with N<sub>2</sub>-O<sub>2</sub> shielding. Plasma Sources Science and Technology, In press, 10.1088/1361-6595/ad4054 . hal-04559740

**HAL Id: hal-04559740**

**<https://hal.science/hal-04559740>**

Submitted on 25 Apr 2024

**HAL** is a multi-disciplinary open access archive for the deposit and dissemination of scientific research documents, whether they are published or not. The documents may come from teaching and research institutions in France or abroad, or from public or private research centers.

L'archive ouverte pluridisciplinaire **HAL**, est destinée au dépôt et à la diffusion de documents scientifiques de niveau recherche, publiés ou non, émanant des établissements d'enseignement et de recherche français ou étrangers, des laboratoires publics ou privés.

# Ar( $1s_5$ ) density in a co-axial argon plasma jet with N<sub>2</sub>-O<sub>2</sub> shielding

Duarte Gonçalves<sup>1,2</sup>, Gérard Bauville<sup>1</sup>, Pascal Jeanney<sup>1</sup>, Mário Lino da Silva<sup>2</sup>, Luís Lemos Alves<sup>2</sup>, Stéphane Pasquiers<sup>1</sup>, and João Santos Sousa<sup>1</sup>

<sup>1</sup>Université Paris-Saclay, CNRS, Laboratoire de Physique des Gaz et des Plasmas, France

<sup>2</sup>Instituto de Plasmas e Fusão Nuclear, Instituto Superior Técnico, Universidade de Lisboa, Portugal

March 5, 2024

## Abstract

Atmospheric-pressure microplasma jets ( $\mu$ APPJs) are versatile sources of reactive species with diverse applications. However, understanding the plasma chemistry in these jets is challenging due to plasma-flow interactions in heterogeneous gas mixtures. Local Ar( $1s_5$ ) density profiles from pure N<sub>2</sub> to pure O<sub>2</sub> shielding provide insights into physical and chemical processes. This work focuses on controlling the shielding gas around a  $\mu$ APPJ. We use a dielectric barrier discharge co-axial reactor where a co-flow shields the pure argon jet with different N<sub>2</sub>-O<sub>2</sub> gas mixtures. A voltage pulse (4 kV, 1  $\mu$ s duration, 20 kHz) generates a first discharge at the pulse's rising edge and a second discharge at the falling edge. Tunable diode laser absorption spectroscopy measures the local Ar( $1s_5$ ) density. A pure N<sub>2</sub> (100%N<sub>2</sub>-0%O<sub>2</sub>) co-flow leads to less reproducible and lower peak Ar( $1s_5$ ) density ( $5.8 \times 10^{13} \text{ cm}^{-3}$ ). Increasing the O<sub>2</sub> admixture in the co-flow yields narrower Ar( $1s_5$ ) absorbance profiles and increases the Ar( $1s_5$ ) density ( $6.9 \times 10^{13}$  -  $9.1 \times 10^{13} \text{ cm}^{-3}$ ). The position of the peak density is closer to the reactor for higher O<sub>2</sub> fractions. Absence of N<sub>2</sub> results in comparable Ar( $1s_5$ ) densities between first and second discharges (maxima of  $9.1 \times 10^{13}$  and  $9.3 \times 10^{13} \text{ cm}^{-3}$ , respectively). The spatially-resolved data may contribute to optimising argon  $\mu$ APPJ reactors across the various applications and to validate numerical models.

## 1 Introduction

Low-temperature atmospheric-pressure microplasma jets ( $\mu$ APPJs) extend plasma beyond physical barriers, providing a controlled method of plasma delivery [1].  $\mu$ APPJs applications benefit from their portability and flexibility of gas mixtures, influencing the associated chemistry. The access to non-equilibrium plasma chemistry at ambient pressure (1 atm) and close to ambient temperature renders these plasma sources attractive for a range of applications, including biomedical [2–4], chemical analysis [5–7], material processing [8–10], and other industries [11].

$\mu$ APPJs can be created by repeated pulsed dis-

charges producing streamers [12] or ionization waves (IW) [13]. The gas jet is usually composed of a noble gas, such as helium [14–21], the cost-effective argon [6, 22–28], or neon [29]. These gases help to guide the ionisation wave downstream from the plasma reactor's nozzle and along the jet axis [30, 31]. Accordingly, although the flow transports reactive species from the reactor into the quiescent air, the IWs are responsible for locally exciting and ionising species along the gas jet.

Noble gases also help to produce cooler plasma jets. Compared to molecular gases, like N<sub>2</sub> and O<sub>2</sub>, noble gases allow a lower operating gas temperature [32] by exhibiting energy transfer rates from electronically excited states to the gas translation mode lower than those observed from vibrationally and rotationally excited states of molecules. Moreover, noble gases facilitate breakdown at lower reduced electric fields due to higher energy tails in the electron energy distribution function (low-energy electronically and vibrational excited states of N<sub>2</sub> and O<sub>2</sub> deplete the tail), reduced recombination rates, and the occurrence of low-energy ionisation processes through step-wise ionisation of metastable states [33]. Even so, there is considerable energy stored in the plasma due to the presence of highly excited species (e.g. Ar\* at 11.55-15.75 eV), which contribute to producing reactive oxygen and nitrogen species relevant for applications.

The unconfined nature of a plasma jet leads to interactions with the surrounding environment. In an argon  $\mu$ APPJ, Gazeli *et al.*[24] showed varying metastable density and lifetime with different gas flow rates. A high flow rate might induce turbulence, subsequently influencing the trajectory of the IWs [34] and increasing the quenching of excited species due to an enhanced mixing [35, 36]. The geometry of the reactor can also influence the IWs [11, 19, 33], potentially giving rise to plasma-induced flow perturbations [37, 38]. In co-axial reactors, factors like nozzle shape, flow rate, and co-flow rate are crucial in determining turbulence and gas mixing [39]. Moreover, in such reactors, one can manipulate the nature of the shielding gas, affecting the production of reactive species [40, 41]. Lastly, electric parameters directly impact the IW. The shape of the

voltage-pulse significantly influences the production of reactive species [15], and the amplitude of the voltage-pulse and frequency affect the reproducibility of the discharge [42–45].

Certain combinations of the previous factors can cause this transient system to reach a periodic stationary state [46], in which the trajectory of IWs is highly reproducible from pulse to pulse. This scenario is typically observed in helium APPJs, whereas it is less prevalent in argon, where IWs become filamentary in certain conditions [7, 22, 47]. Filamentary IWs exhibit thinner streamers and a higher branching rate, challenging experimental measurements. Nevertheless, electric parameters can be adjusted to produce reproducible IWs in argon APPJs [7, 22]. Several studies have successfully measured fundamental quantities such as electron density and electric field [33] (Stark broadening [48–51], Thomson scattering [52–54]), as well as density and temperature of heavy chemical species, using emission and absorption spectroscopy [55, 56].

Tunable diode laser absorption spectroscopy (TDLAS) is a non-intrusive diagnostic that allows for time- and space-resolved absolute density of species [56]. In argon  $\mu$ APPJs, this diagnostic has been applied to measure the density of 4s states using line-of-sight or Abel inverse transform of the absorbance [22–24, 26, 28, 47, 57–59]. In particular, the 811.531 nm line for the radiative transition  $\text{Ar}(2p_9 \rightarrow 1s_5)$  can be used to probe the density of  $\text{Ar}(1s_5)$ . Schroter *et al.* [58] determined line-of-sight densities of  $\sim 10^{14} \text{ cm}^{-3}$  in a 22 kHz argon- $\text{N}_2$  APPJ. Various studies have examined argon  $\mu$ APPJs excited by a bell-shaped voltage pulse operating at 20 kHz and maximum amplitude of 6 kV [6, 7, 23, 24, 37]. These electric conditions allowed for reproducible IWs with a characteristic diffuse light emission [22]. These reactors’ reproducible IWs are obtained for an argon flow rate above 400 sccm and below 1100 sccm, applied voltage above 4 kV, and frequency above 10 kHz. Using a free-jet configuration at a 750 sccm flow rate, Es-sebbar *et al.* [22] obtained an  $\text{Ar}(1s_5)$  density of  $2.5 \times 10^{13} \text{ cm}^{-3}$ ,  $\sim 4.8 \text{ mm}$  from the nozzle using the line-of-sight method. Gazeli *et al.* [23] performed an Abel inversion of the peak absorbance profile in highly symmetric regions, resulting in an  $\text{Ar}(1s_5)$  maximum density ranging from  $1 \times 10^{13}$  to  $2 \times 10^{14} \text{ cm}^{-3}$  for glass and alumina targets, respectively.

In this work, we build on previous research efforts to characterise  $\mu$ APPJs, measuring the spatial profile of the maximum  $\text{Ar}(1s_5)$  density. By controlling the shielding gas mixture, we quantify how it affects the  $\text{Ar}(1s_5)$  density, providing hypotheses that relate to the plasma behaviour and fluid dynamic effects.

We use a co-axial cylindrical dielectric barrier discharge (DBD) reactor to produce an argon plasma jet (1 slm main jet, 3 slm  $\text{N}_2\text{-O}_2$  co-flow) by applying a square voltage pulse (4 kV amplitude, 20 kHz frequency, 1  $\mu\text{s}$  long, 85 ns rise and 115 ns fall time). An in-house power source generates high-fidelity square pulses, producing two discharges, one at the rising edge

and another at the falling edge of the applied voltage pulse. Both discharges are investigated with different shielding flow mixtures of  $\text{N}_2$  and  $\text{O}_2$  using a TDLAS setup similar to previous works [21–24, 60]. The current enables high spatial (28  $\mu\text{m}$  horizontally and 48  $\mu\text{m}$  vertically) and temporal (3 ns) resolution of the absorbance. Together with various data processing methods, this allows determining space-resolved absolute densities of  $\text{Ar}(1s_5)$ . The different shielding gas mixtures allow one to isolate physical and chemical effects related to  $\text{Ar-N}_2\text{-O}_2$  chemistry.

This paper continues with Section 2, describing the materials and methods: first, the reactor setup, the gas flow parameters, and the power source are presented; then, the TDLAS experimental setup is outlined; the methods of laser absorption spectroscopy and data processing and analysis are described; and finally, the computational fluid dynamics methods are described. Section 3 presents the results and discussion describing computational fluid modelling results; laminar-turbulent jet characteristics; co-flow rate effect on  $\text{Ar}(1s_5)$  density; the reproducibility of  $\text{Ar}(1s_5)$  density values; and spatial profiles of the peak  $\text{Ar}(1s_5)$  density. Section 4 concludes with a summary.

## 2 Material and methods

### 2.1 Reactor setup

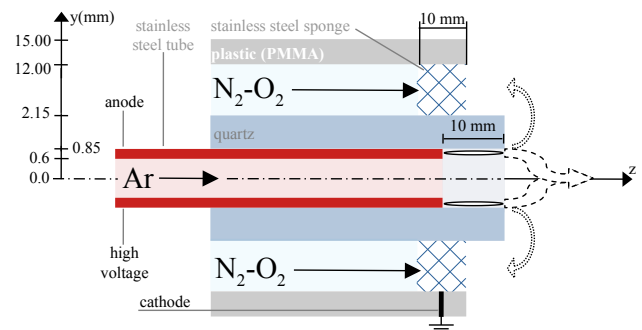


Figure 1: Scheme of the co-axial reactor including relevant dimensions. The origin of the transverse axis,  $y$ , is at the reactor’s centre line, and the axial axis’s origin,  $z$ , is at the nozzle exit. Solid-line ellipses are a possible position for surface charges and the initial surface DBD. Dashed-line arrows represent the IW’s trajectory while leaving the nozzle. The expected electrostatic field lines outside the nozzle are in dotted-line arrows in a case without discharge.

We use a cylindrical DBD reactor with an exposed electrode; see Figure 1. This reactor produces an initial surface DBD (schematically represented in solid-line ellipses in the figure), inducing a guided IW along the jet. The reactor comprises a stainless steel tube, acting as the high-voltage electrode (anode), which is mechanically forced inside a quartz tube. A stainless steel sponge, the grounded electrode (cathode), sits between the quartz tube and a plastic (PMMA) tube. Ar-

gon flows from inside the stainless steel tube into the quartz tube, creating the main jet on exit. An  $\text{N}_2\text{-O}_2$  gas mixture flows between the quartz and the plastic tubes and through the stainless steel sponge, where it exits, creating the co-flow shielding jet.

## 2.2 Flow conditions

For the main jet, a thermal mass flow controller (GF40-SA46 from Brooks Instrument) maintains a 1 slm flow rate of argon (from AirLiquide, AlphaGaz 1,  $\text{Ar} \geq 99.999\%$ , impurities in mole fractions:  $\text{H}_2\text{O} \leq 3$  ppm,  $\text{O}_2 \leq 2$  ppm,  $\text{C}_n\text{H}_m \leq 0.5$  ppm). For the co-axial jet, we explored a range of flow rates. Using Schlieren imaging, we found that a co-flow flux above 5 slm and below 2 slm is unsteady, and a flux of at least 2 slm is necessary to shield the argon jet's laminar portion fully. A flux between 3 slm and 4 slm led to more reproducible  $\text{Ar}(1s_5)$  absorbance profiles. Accordingly, we chose a total flux of 3 slm for the co-axial jet, which is set by two thermal flow controllers (red-y compact series, vögtlin): one for the oxygen gas (from AirLiquide, AlphaGaz 1,  $\text{O}_2 \geq 99.995\%$ , impurities in mole fractions:  $\text{H}_2\text{O} \leq 2$  ppm,  $\text{CO}_2 \leq 0.5$  ppm,  $\text{CO} \leq 0.5$  ppm,  $\text{C}_n\text{H}_m \leq 0.5$  ppm) and another for the nitrogen gas (from AirLiquide, AlphaGaz 1, impurities in mole fractions,  $\text{N}_2 \geq 99.999\%$ ,  $\text{H}_2\text{O} \leq 3$  ppm,  $\text{O}_2 \leq 2$  ppm,  $\text{C}_n\text{H}_m \leq 0.5$  ppm). To reduce air and water impurities inside the reactor [60], the jet flow runs for 30 min before acquiring measurements.

## 2.3 Power source

The power source creates a square-shaped voltage pulse. In this work, we apply voltage pulses with an amplitude of 4 kV, frequency of 20 kHz, and pulse duration set to  $1\mu\text{s}$ , with its full width at half maximum of  $1.044\mu\text{s}$ . For these conditions, the rise and fall times of the pulse are  $\sim 85$  ns and 115 ns, respectively.

At 20 kHz and 4 kV, the reactor takes about 20 min to heat up to a stable temperature, with the plastic tube and the quartz reaching  $2^\circ\text{C}$  above room temperature and the stainless steel tube reaching  $5^\circ\text{C}$  above room temperature (measurements made using an IR camera). The power source also heats up ( $70^\circ\text{C}$ ) during the first 30 minutes of operation, causing the pulse duration to reduce slightly ( $\sim 4\%$  decrease) before attaining a stable value. Accordingly, the power source runs for at least 30 minutes before measurements are acquired.

Each pulse produces two discharges, one during the rising and another during the falling edge of the pulse. Each discharge produces  $\text{Ar}(1s_5)$  metastables along the jet. The  $\text{Ar}(1s_5)$  absorbance decreases to noise levels after  $1\mu\text{s}$ , see Figure 4. Accordingly, we chose a pulse duration of  $1\mu\text{s}$  to decouple the absorbance profiles of the two discharges.

The applied voltage, displacement current, and discharge current are described in Figure 4 over one applied pulse. The applied voltage was measured with a voltage probe (MK-14KVAC from Lecroy), and the

total current was measured with a current transformer (CT-B5.0 from Magnelab). The signal's waveform was acquired using a 2 GHz bandwidth digital oscilloscope (Lecroy 204MXi). The capacitance of the reactor was measured to be 0.7 pF.

## 2.4 Laser absorption spectroscopy setup

The current laser absorption spectroscopy setup is similar to previous works [6, 22–24] (please see Es-sebbar *et al.* [22] Figure 1 for a scheme). We used a tunable diode laser (DL100, TOPTICA photonics), in which the temperature and current are set to produce a beam of 811.523 nm wavelength.

After exiting the laser diode, the beam passes through: a neutral density filter to attenuate its intensity; a motorised shutter; a circular diaphragm to shape it; two mirrors to reflect it into the jet's  $x$ -axis (see Figure 2) and a second diaphragm to reduce its width. Afterwards, a lens (35 mm focal length) focuses the laser into a narrower width, at which point it transverses the plasma jet. Then, two lenses (35 mm followed by 50 mm focal length) refocus the beam into a silicon photodiode (DC 125 MHz, Model 1801, New Focus), which measures its intensity. A band-pass filter of  $810\pm 10$  nm (810FS-25 Andover Corporation) is placed before the detector to block less relevant wavelengths. The beam waist was measured with the blade edge method [23]. At the point it crosses the jet, the beam intensity varies from 90% and 10% over a distance  $\Delta y = 28\mu\text{m}$  and  $\Delta z = 48\mu\text{m}$  along the transverse and longitudinal directions, respectively, with a sigmoid-like intensity profile. At the lowest aperture, the second diaphragm did not allow for a  $\Delta y < 30\mu\text{m}$  beam waist, needed to resolve the absorbance with  $20\mu\text{m}$  spatial steps. The current beam-waist was achieved by  $y$ -direction diaphragm displacement, slightly slicing the laser beam along this direction. The  $y, z$  beam-waist difference is not problematic considering that the  $z$ -step (2 mm) is much larger (100 times) than the  $y$ -step ( $20\mu\text{m}$ ).

With the optical setup fixed, two servo micrometre motors move the plasma reactor in the  $y-z$  plane; see Figure 2. We use a 2 mm step in the  $z$  direction and a  $20\mu\text{m}$  step in the  $y$  direction. A computer program controls the stepper motors, the motorised shutter, and data storage from the oscilloscope.

## 2.5 Laser absorption spectroscopy methods

We measured the density of the metastable  $\text{Ar}(1s_5)$  using laser absorption spectroscopy. In our setup, the laser beam, set at the wavelength of the  $\text{Ar}(2p_9)\rightarrow\text{Ar}(1s_5)$  transition  $\lambda_0 = 811.531$  nm, passes through the plasma and hits the photodiode detector. While passing through the jet, the variation of the intensity is related to the density of the absorbing species by the Beer-Lambert law:

$$I(\lambda_0, y) = I_0(\lambda_0) e^{-\int_0^L k(\lambda_0, x, y) dx}, \quad (1)$$

where  $\lambda_0$  is the absorption wavelength,  $I_0$  is the original beam intensity,  $I$  is the intensity after travelling a distance  $L$  through the absorbing medium, and  $k(\lambda)$  is the absorption coefficient. This relation can be written as

$$\int_0^L k(\lambda_0, x, y) dx = -\log\left(\frac{I(\lambda_0)}{I_0(\lambda_0)}\right) = \rho(\lambda_0, y), \quad (2)$$

where  $\rho(\lambda_0, y)$  is the absorbance at a specific wavelength  $\lambda_0$ , see Figure 2.

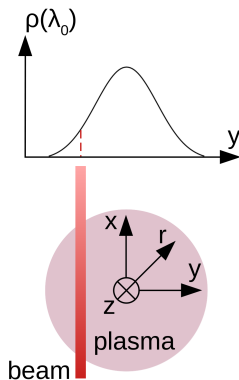


Figure 2: Schematic of the laser passing through the plasma, including the referential. Representative absorbance profile along the transverse direction. Stepper motors move the reactor along the transverse direction  $y$  and the axial direction  $z$ .

The absorbance was generally axisymmetric in our  $\mu$ APPJ; see section 3. In this cylindrical geometry, see Figure 2, the Abel transform can provide a relation between the absorption coefficient and the absorbance,

$$k(\lambda_0, r) = -\frac{1}{\pi} \int_r^\infty \frac{\partial \rho(\lambda_0, y)}{\partial y} \frac{dy}{\sqrt{y^2 - r^2}}. \quad (3)$$

For an atomic line, the absorption coefficient reads [61],

$$k(\lambda_0, r, z) = \frac{e^2}{4\epsilon_0 m_e c} f_{ij} P(\nu_0) n(r, z), \quad (4)$$

where we added the dependence in  $z$ , and where  $e$  is the elementary charge,  $f_{ij}$  is the oscillator strength for the line,  $\epsilon_0$  is the vacuum permittivity,  $c$  is the vacuum speed of light,  $n$  is the number density of the atomic species absorbing the light,  $\nu_0$  the frequency of the laser beam, and  $P(\nu)$  is the normalized line profile ( $\int P(\nu) d\nu = 1$ ).

If the normalized line profile has a Lorentzian shape, it can be described as a function of the full width at half maximum (FWHM), having units inverse of its domain [62]. At its peak, at a frequency  $\nu_0$ , the maximum

is given  $P(\nu_0) = 2/(\pi \Delta\nu_L)$ , with  $\Delta\nu_L$  the (FWHM). Using this profile on equation 4, the  $\text{Ar}(1s_5)$  density can be calculated from

$$n(r, z) = \frac{2\pi\epsilon_0 m_e c}{e^2 f_{ij}} \Delta\nu_L k(\lambda_0, r, z). \quad (5)$$

## 2.6 $\text{Ar}(1s_5) \rightarrow \text{Ar}(2p_9)$ line absorption profile

For an atomic transition, the absorption profile can be broadened by multiple processes [56, 63, 64]. Various broadening mechanisms are a function of the gas temperature. Although we did not measure the gas temperature, previous works using a similar reactor with a different power source [22–24] measured a maximum gas temperature of up to 350 K. In the following, we estimate the broadening by different processes.

The FWHM of the natural broadening is given by  $\Delta\lambda_{\text{Natural}} = \lambda_0^2 A / (2\pi c) = 0.01$  pm [64], where  $A = 3.3 \times 10^7 \text{ s}^{-1}$  [65] is the Einstein coefficient of the transition.

The FWHM of the Doppler broadening is  $\Delta\lambda_D = \lambda_0 2\sqrt{2 \log 2} \sqrt{k_B T_g / mc^2} = 1.59$  pm [56, 66], where  $T_g = 300$  K is the gas temperature,  $k_B$  the Boltzmann constant, and  $m$  is the mass of an argon atom. Considering a gas temperature of 350 K, the FWHM increases by 8% at most.

From previous works in argon  $\mu$ APPJs, using a similar reactor but with a bell-shaped applied voltage of amplitude 6 kV and 20 kHz (identical to the applied voltage used in [22]), the electron density reached at maximum  $n_e = 2 \times 10^{14} \text{ cm}^{-3}$  and the electron temperature corresponded to  $T_e \approx 2.9 \times 10^4$  K [54]. This leads to an upper estimate for the FWHM of the Stark broadening of  $\Delta\lambda_{\text{Stark}} = (1.05 \times 10^{-4} T_e + 4.86) \frac{n_e [\text{cm}^{-3}]}{10^{16}} = 0.16$  pm [67].

The FWHM of the van der Waals broadening can be written as [63, 68],

$$\Delta\lambda_{\text{vdW}} = 8.18 \times 10^{-22} \lambda_0^2 (\bar{\alpha} \bar{R}^2)^{2/5} \left(\frac{T_g}{\mu}\right)^{0.3} N = 39.55 \text{ pm},$$

where  $\bar{\alpha}$  is the mean atomic polarizability,  $\bar{R}^2$  is the difference of the squares of the coordinate vectors of the upper and lower levels,  $T_g = 300$  K is the gas temperature,  $\mu$  is the reduced mass, and  $N$  is the gas density. Konjević [68] provides the various parameters for argon-argon broadening. In the case of  $T_g = 350$  K, the van der Waals broadening would increase by 10%. Considering instead  $\text{N}_2$  or  $\text{O}_2$  perturbers, the van der Waals broadening would be 40.96 pm or 41.51 pm, respectively, were the polarizabilities of  $\text{N}_2$  and  $\text{O}_2$  were obtained from [69]. The FWHM of two convoluted Lorentzian profiles is given by the sum of the FWHM of the individual Lorentzian profiles. Accordingly, assuming a 80% (99%) Ar mixture with dry-air, the FWHM of the van der Waals broadening would increase to 39.85 (39.57) pm, which is not as significant as the effect of the gas temperature.

Experimentally, the absorption profile was determined by varying the temperature of the tunable laser, which yields a linear variation of its wavelength [24]. Both the Voigt and Lorentzian profiles fit the absorption profile well. The former estimates the Gaussian variance at zero, probably due to the low contributions from Gaussian-like broadenings. The Lorentz fit, see Figure 3, converges in a FWHM  $\Delta\lambda_L = 40.10 \pm 0.52$  pm, or  $\Delta\nu_L = 18.27 \pm 0.24$  GHz (centred at 811.531 nm), which according to the previous estimates can be mainly attributed to van der Waals broadening. At 5 mm from the nozzle, between cases with a dry-air shielding co-flow and without co-flow, and between the centre and the edge of the plasma jet, the FWHM varied at most by 7%. Accordingly, a constant  $\Delta\nu_L = 18.27$  GHz value is used for the density calculations.

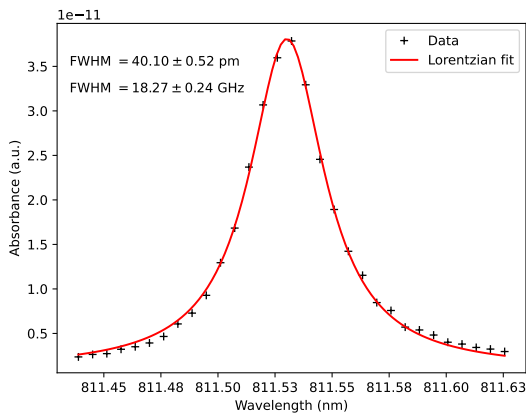


Figure 3: Normalised line absorption profile ( $P(\nu)$ ,  $\int P(\nu)d\nu = 1$ ) at 5 mm from the nozzle and at the centre of the plasma jet with a dry-air co-flow at 3 slm co-flow rate. The profile was fitted to a Lorentzian function with a constant baseline.

## 2.7 Data acquisition and processing

The oscilloscope records the electric signals (applied voltage, current, and transmitted light measured by the photodiode). Both current and transmitted light signals are corrupted by electromagnetic noise produced by the open plasma reactor. The transmitted light signal's noise was digitally removed by subtracting a noise baseline produced with the laser off.

For each voltage pulse and each  $(y, z)$  position, the temporal of the transmitted light signal contains two minima corresponding to the Ar( $1s_5$ ) metastable production for each of the two discharges. The oscilloscope then stores 1000 values of the two minima of the transmitted light, one full temporal profile of the transmitted light, the applied voltage, and the total current. The transmitted light minima corresponds to the maxima of absorbance. Using the 1000 maximum absorbance values, we compute the median (50th percentile), relative standard deviation (RSD), and 5th

and 95th percentiles. The RSD can be computed as,

$$\text{RSD}(y, z) = \frac{\sqrt{\frac{1}{1000} \sum_{i=1}^{1000} [A_i(y, z) - \mu(y, z)]^2}}{\mu}, \quad (6)$$

where  $A_i(y, z)$  the maximum absorbance for the pulse  $i$  at the position  $(y, z)$  and  $\mu(y, z)$  is the arithmetic mean. This metric indicates higher or lower variation between pulses; see Figure 9. However, in specific conditions, such as those near the nozzle, the distribution of the 1000 maximum absorbance values deviates significantly from a normal distribution. In such cases, the 5th, 50th (median), and 95th percentiles of the 1000 maximum absorbance values describe the dispersion better. Using the median of the 1000 values of maximum absorption for each  $(y, z)$  position, one obtains 2D maps for the maximum absorbance for each of the two discharges.

The inverse Abel transform is used to obtain the Ar metastable density radial profile from the transverse profiles. We compared the algorithms available in PyAbel [70] to that of Beniaminy and Deutsch [71] used in previous  $\mu$ APPJ works [23, 60]. A Gaussian function, for which an analytical inverse Abel transform exists, served as a benchmark. For this analytical function, we defined various discrete Gaussian profiles with different standard deviations and number of points and applied each Abel transform algorithm. The methods that yielded solutions closest to the analytical were the Basex16 and that of Beniaminy and Deutsch. We chose the former due to performing better at fewer points.

We perform an inverse transform of the left- and the right-hand side of the transverse profiles. By comparing the two profiles, one can evaluate if the transform profile is symmetric, a condition for the validity of the Abel transform. The left- and right-hand side inverted profiles should be continuous at  $r = 0$ , but it was not always possible to measure the absorbance at the centre of the profile. The reason is twofold. First, the reactor was mounted at an angle to the rail of the axial micrometre motor. Second, to correct this fault in the setup, the rail was slightly tilted to place the reactor perpendicularly to the table holding the laser. After this correction, when moving the reactor to acquire transverse absorbance profiles at different axial positions, the centre of the region under analysis is horizontally displaced by tens of  $\mu\text{m}$ . Accordingly, we define the centre by interpolating the transverse signal with a second-order spline and by iteratively calculating the position of the centre using a Newton-Raphson algorithm (tolerance of  $35 \mu\text{m}$ ), until the left and right radial profiles are continuous at  $r = 0$ . In a few cases of transverse profile asymmetry, the algorithm cannot converge; these cases are identified in the results section.

## 2.8 Computational fluid dynamic simulations

Computational fluid dynamics simulations described the Ar molar fractions along the jet. We used a sub-

sonic version of the Simulation Platform for Aerothermodynamics Radiation and Kinetics (SPARK) [72], a finite-volume code solving the compressible Navier-Stokes equations. The subsonic version of SPARK differs from the original by including low-Mach preconditioning [73], the simple low-dissipation advection upstream splitting method (SLAU) inviscid flux solver [74], and primitive variables reconstruction using WENO-5 [75]. The diffusive flux coefficients are calculated from the Wilke-Blottner-Eucken model as described in [76], where viscosity coefficients were obtained from [77].

Simulations are performed for a 2D axisymmetric geometry. The simulation domain adopted the reactor's dimensions extended until 40 mm longitudinally and 14 mm radially. We assume a parabolic velocity profile with a gas temperature of 300 K for the main central jet and the co-flow jet. A no-slip condition is assumed at the walls, a symmetry condition at the axis, and elsewhere, we adopt a subsonic outlet at a static pressure of 101325 Pa. A sponge layer between 33 mm and 40 mm damps possible acoustic waves. Convergence was assumed once the flow variables remained stationary and after a drop of  $10^{-3}$  in the total residuals.

### 3 Results and discussion

#### 3.1 Electric signals and absorbance

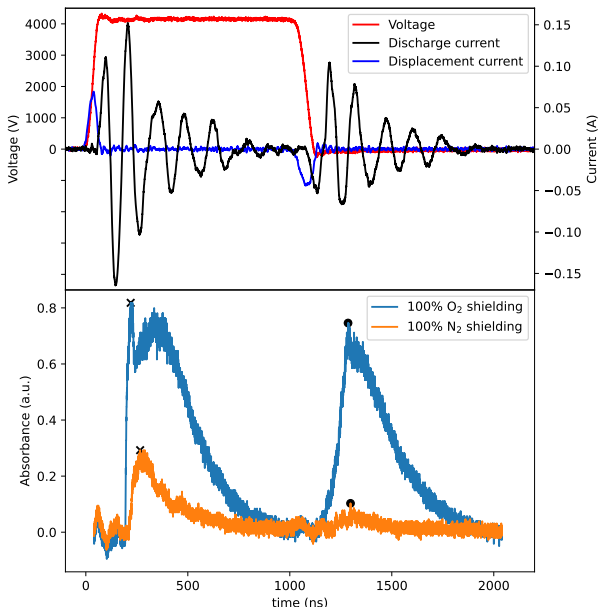


Figure 4: Applied voltage pulse, discharge and displacement current, and absorbance temporal profiles during the pulse. Measured at  $z = 10$  mm and  $y = 0$   $\mu$ m for 100%N<sub>2</sub> (orange) and 100%O<sub>2</sub> (blue) shielding gas. Absorbance starts to increase during the passage of the streamer, which at  $z = 10$  mm is at  $\sim 200$  ns (varying with the shielding gas mixture) after the start of the discharge. The maximum absorbance is marked for each discharge:  $\times$  the first discharge;  $\bullet$  the second discharge.

Our cylindrical DBD reactor, see Figure 1, produces two discharges per applied voltage pulse, each one producing Ar(1s<sub>5</sub>) species, see Figure 4. This figure shows the time evolution of the discharge current and the plasma absorbance over one applied voltage pulse. The discharge current and the absorbance present two peaks: one during the rising edge and another on the falling edge of the applied voltage pulse. Fast imaging diagnostics show an IW propagating downstream along the jet after the first current peak, which is consistent with previous works using a bell-shaped applied pulse [6, 22–24]. During the plateau of the applied pulse, the discharge current oscillations decrease to almost null amplitude, which is coherent with the behaviour of a DBD reactor where surface charges deposited on the dielectric cancel out the electric potential difference to the anode. The surface charges are subsequently released upon the decrease in the applied voltage during the falling edge of the pulse. This produces a second discharge, which also propagates downstream. While the first discharge is an IW, being filamentary or diffuse depending on the position along the argon jet [22], the second discharge is always diffuse. The propagation of the ionisation wave downstream along the argon jet, see Figure 1, should be related to the plasma electronegative shielding [31, 60], where anions clustering around the jet reduce the conductivity in the jet/shielding boundary, thus focusing the IW into the centre of the jet. Although this mechanism is usually associated with IWs (the first discharge in our case), it should also be present in the second discharge, starting only  $1\mu$ s after the IW. For a 100% N<sub>2</sub> shielding gas, see Figure 4, the Ar(1s<sub>5</sub>) density is particularly low, suggesting a less effective electronegative shielding due to a much lower anion production.

#### 3.2 Computational fluid dynamic simulations

Since the mixing rates between the argon jet and the co-flow gas may influence the IW trajectory and the quenching rates of Ar(1s<sub>5</sub>), we performed CFD simulations to evaluate the Ar molar fraction for the different shielding gas mixtures. In laminar flows, the mixing depends mainly on the diffusion coefficients, or equivalently, the viscosity of the gas [78], which is comparable for N<sub>2</sub>, O<sub>2</sub>, and humid air with 2%H<sub>2</sub>O [79]. Still, gaseous oxygen is slightly more viscous than nitrogen, leading to a faster mixing with the argon jet and lower axial argon fraction. However, at the axis, between 100%N<sub>2</sub> and 100%O<sub>2</sub> shieldings, the relative difference in Ar molar fraction is low: 1% at 12 mm, 5% at 22 mm, and 10% at 33 mm. The mixing starts from the jet/shielding boundary towards the jet's inside. If we delimit the locations with a 90% (99%) Ar mole fraction, we obtain a cone-like shape of about 20 mm (10 mm) in length, see Figure 5. Accordingly, contour regions of higher argon fractions are cone-shaped, with smaller areas for higher argon purity. This is consistent with the cone-shaped density profiles of argon metastables measured in this work with TDLAS.

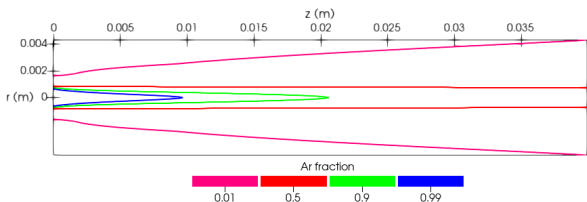


Figure 5: Contours of the Argon molar fraction in the case of no co-flow, i.e. pure argon jet into a quiescent dry-air + 2% $\text{H}_2\text{O}$  gas mixture.

### 3.3 Laminar to turbulent flow transition

Complementary Schlieren imaging was performed to evaluate the laminar length of the argon jet. These experiments were performed in an identical experimental setup to the work of Darny *et al.* [37]. Without plasma and in the absence of co-flow (no co-flow), images show a laminar and almost cylindrical argon jet flowing from the nozzle, which eventually transitions into a turbulent flow at about  $39.4 \pm 2.2$  mm from the nozzle. Without plasma and with co-flow, a shielding gas envelopes the argon jet, starting from the edge of the co-flow tube until the turbulent region. In this case, the average laminar length is of:

- $40.05 \pm 2.65$  mm, for a 100% $\text{N}_2$ /0% $\text{O}_2$  shielding;
- $35.15 \pm 2.10$  mm, for an 80% $\text{N}_2$ /20% $\text{O}_2$  shielding;
- $33.30 \pm 1.50$  mm, for a 50% $\text{N}_2$ /50% $\text{O}_2$  shielding;
- $34.20 \pm 1.05$  mm, for a 20% $\text{N}_2$ /80% $\text{O}_2$  shielding;
- $34.90 \pm 1.15$  mm, for a 0% $\text{N}_2$ /100% $\text{O}_2$  shielding.

The decrease in laminar length points to a more unstable jet for higher oxygen-fraction shieldings. Although we did not perform Schlieren measurements for a 4 kV pulse, for a 6 kV and 500 ns pulse duration at 20 kHz, the average laminar length was reduced by:

- $\sim 8$  mm without co-flow shielding;
- $\sim 7$  mm for 100% $\text{N}_2$ /0% $\text{O}_2$  shielding;
- $\sim 8$  mm for 80% $\text{N}_2$ /20% $\text{O}_2$  shielding;
- $\sim 10$  mm for 50% $\text{N}_2$ /50% $\text{O}_2$  shielding;
- $\sim 14$  mm for 20% $\text{N}_2$ /80% $\text{O}_2$  shielding;
- $\sim 16$  mm for 0% $\text{N}_2$ /100% $\text{O}_2$  shielding.

The decrease in laminar length with plasma ON is expected as plasma-flow perturbations have been shown to disrupt the laminar flow [37, 38]. Higher oxygen-fraction shieldings also seem to enhance plasma-flow perturbations, although this effect may be due to an already more unstable jet, as described in the plasma OFF case. A lower laminar length may affect the  $\text{Ar}(1s_5)$  density profiles due to the increased mixing, leading to a higher  $\text{Ar}(1s_5)$  quenching rate. In the case of an air shielding, the quenching rates of relevant species are (in units of  $10^{-11} \text{ cm}^3 \text{ s}^{-1}$ ) of 3.6 in  $\text{N}_2$  [80], 21 in  $\text{O}_2$  [80] and 78 in  $\text{H}_2\text{O}$  ([59]).

### 3.4 $\text{Ar}(1s_5)$ density for increasing dry-air co-flow rate

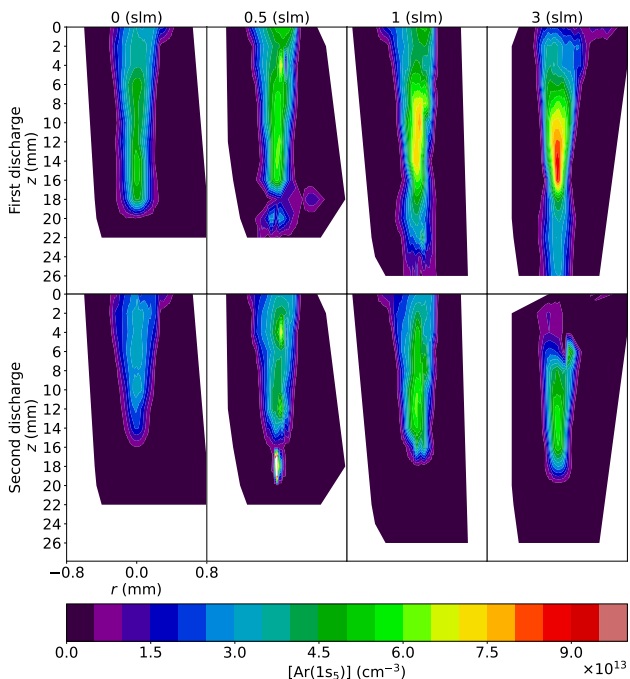


Figure 6: Spatial profiles of the maximum  $\text{Ar}(1s_5)$  density at different  $(r, z)$  positions for the first discharge (first row) and the second discharge (second row), and for different dry-air co-flow rate (depicted in different columns). Negative radial positions are for data obtained from Abel inversion of the left-hand side of the transverse absorbance profile, while positive radial positions are for the corresponding right-hand side. Comparison between profiles at negative and positive radii allows for estimating the symmetry of the absorbance and thus the reliability of the  $\text{Ar}(1s_5)$  density measurement.

Our TDLAS setup and methods allow us to measure for each point  $(r, z)$ , the maximum  $\text{Ar}(1s_5)$  density of the first and second discharges, which can be displayed in the form of 2D maps for the whole jet, as shown in Figure 6.

For the first discharge, without co-flow, the spatial profile of the  $\text{Ar}(1s_5)$  density is cylindrical with increasing values density along  $z$  up to  $5.2 \times 10^{13} \text{ cm}^{-3}$  at 14 mm from the nozzle, decreasing to below  $1 \times 10^{13} \text{ cm}^{-3}$  at 20 mm. With a 0.5 slm dry-air co-flow, the maximum density increases in the jet's centre, reaching a maximum value of  $7.2 \times 10^{13} \text{ cm}^{-3}$  at 4 mm from the nozzle. The profile becomes shorter (densities around  $1.5 \times 10^{13} \text{ cm}^{-3}$  near 18 mm) and less symmetric. Increasing to a 1 slm dry-air co-flow, the maximum density in the jet's centre rises again, reaching a maximum value of  $8.0 \times 10^{13} \text{ cm}^{-3}$  at 10 mm from the nozzle. The profile is more asymmetric, longer (densities around  $1.7 \times 10^{13} \text{ cm}^{-3}$  near 26 mm), and cone-shaped, being broader near the nozzle and narrower at 14 and 16 mm before broadening again at 20 mm. At a 3 slm co-flow rate, the density increases to a maximum

of  $8.9 \times 10^{13} \text{ cm}^{-3}$  at 14 mm. The profile is now symmetric, longer (densities around  $3 \times 10^{13} \text{ cm}^{-3}$  at 26 mm), and cone-like as before, with a narrower position near 16 mm.

The profile is cone-like for the second discharge without co-flow with decreasing density along  $z$ . It reaches a maximum value of  $3.4 \times 10^{13} \text{ cm}^{-3}$  at 6 mm from the nozzle and a minimum value of  $4.6 \times 10^{12} \text{ cm}^{-3}$  at 16 mm from the nozzle. The asymmetry increases for a 0.5 slm dry-air co-flow, where the density increases to  $7.2 \times 10^{13} \text{ cm}^{-3}$  at 4 mm, decreasing to  $7.4 \times 10^{12} \text{ cm}^{-3}$  at 16 mm from the nozzle. With a 1 slm co-flow, the profile is still asymmetric, and the Ar( $1s_5$ ) density reaches a peak value of  $6.3 \times 10^{13} \text{ cm}^{-3}$  around from 12 mm, decreasing to  $3.9 \times 10^{12} \text{ cm}^{-3}$  at 18 mm from the nozzle. With a 3 slm co-flow, the profile becomes symmetric from 8 mm onward, funnelling until 14 mm, which becomes cylindrical. For this co-flow rate, the Ar( $1s_5$ ) density reaches a value of  $5.8 \times 10^{13} \text{ cm}^{-3}$  from 14 mm, decreasing to  $5.7 \times 10^{11} \text{ cm}^{-3}$  at 18 mm from the nozzle.

Dry-air shielding reduces the concentration of  $\text{H}_2\text{O}$  surrounding and in the plasma jet, which may lengthen and broaden the spatial profile of the Ar( $1s_5$ ) maximum density. Compared to dry air, humid air has a higher attachment rate, which can hinder the formation and propagation of the streamer [81, 82] by reducing the accumulation of charges on the streamer head, lowering its radius and velocity and increasing the threshold field for propagation. Also, the quenching rate of Ar( $1s_5$ ) by  $\text{H}_2\text{O}$  is higher than that of  $\text{O}_2$  ( $\sim 4$ -fold) or  $\text{N}_2$  ( $\sim 21$ -fold), see section 3.3, which could lead to lower Ar( $1s_5$ ) peak densities and shorter profiles.

The lower Ar( $1s_5$ ) densities obtained for co-flows of 1 slm and 0.5 slm may result from incomplete shielding, leading to a higher  $\text{H}_2\text{O}$  concentration in the argon jet. The lower densities could also be caused by a non-stationary flow, leading to less reproducible IW trajectories. The asymmetric Ar( $1s_5$ ) density profile for 0.5 and 1 slm co-flows supports this hypothesis, and Schlieren imaging also shows an asymmetric flow pattern in the case of a 1 slm co-flow.

### 3.5 Reproducibility of the absorbance with different $\text{N}_2/\text{O}_2$ co-flow gas fraction

While sweeping the co-flow rate between values of 0.5 slm to 5 slm, we found a higher reproducibility of the Ar( $1s_5$ ) absorbance profile for co-flows between 3 and 4 slm. Accordingly, a 3 slm co-flow rate was used to measure Ar( $1s_5$ ) density between different  $\text{N}_2/\text{O}_2$  co-flow gas fractions.

Oxygen in the co-flow mixture affected the variability and the shape of the absorbance profiles from pulse to pulse; see Figure 7. Near the nozzle, the variability is much higher for both discharges and all co-flow mixtures. Moving away from the nozzle, the variability decreases, remaining higher for a 100% $\text{N}_2$  (0% $\text{O}_2$ )

co-flow, which also shows a broader profile. The admixture of 2%  $\text{O}_2$  in the co-flow is enough to considerably reduce the variability and narrow the profile to shapes similar to those of a 100%  $\text{O}_2$  co-flow mixture.

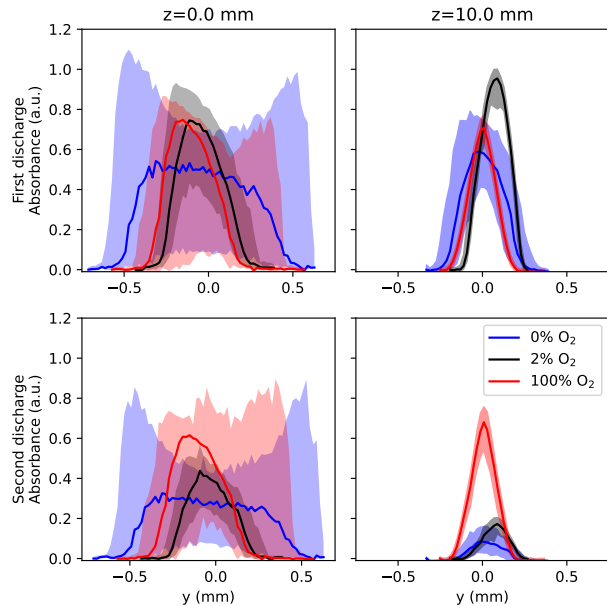


Figure 7: Maximum Ar( $1s_5$ ) absorbance values over 1000 pulses, for different shielding gas mixture (red 100% $\text{O}_2/0\%\text{N}_2$ , blue 0% $\text{O}_2/100\%\text{N}_2$ , black 2% $\text{O}_2/98\%\text{N}_2$ ). Solid lines show the median value of the 1000 measures of maximum absorbance at each ( $y, z$ ) position. The shaded area encompasses values between the 5th and 95th percentiles of the 1000 measures. Top row: first discharge, bottom row: second discharge. Left column:  $z = 0 \text{ mm}$ , right column:  $z = 10 \text{ mm}$ .

Spatial profiles of the RSD of the maximum absorbance are presented in Figure 9. The RSD is always below 40%. The RSD reduces to 15% from 10 mm onwards for co-flows with oxygen and 14 mm onwards for a 100% $\text{N}_2$ (0% $\text{O}_2$ ) co-flow. For the first discharge, the decrease in the RSD coincides with the beginning of the symmetric region for the profiles of the Ar( $1s_5$ ) maximum density, see Figure 10.

The broader absorbance profiles and higher RSD observed for every co-flow mixture of the first discharge near the nozzle can be due to the random trajectory of the streamer as it propagates from the dielectric surface to the axis of the argon jet [31]. These observations are coherent with the hollow electron density profiles measured with Thomson scattering [54] in that region in a similar reactor without co-flow. In our reactor, fast-imaging shows that the ionisation wave is not axisymmetric during the surface-to-volume transition, resembling a thin streamer [22]. This filament leaves the nozzle at varying azimuthal positions from pulse to pulse, which could explain both the high 95th (passing filament) and low 5th (no filament) percentiles of the absorbance values at  $z = 0 \text{ mm}$ , see Figure 8. At the nozzle, the even broader absorbance profile of the

100%N<sub>2</sub> case could be related to a lower electronegative shielding. For higher O<sub>2</sub> concentrations in the co-flow, the narrower profile indicates a better focusing of the ionisation wave [31, 60] closer to the axis.

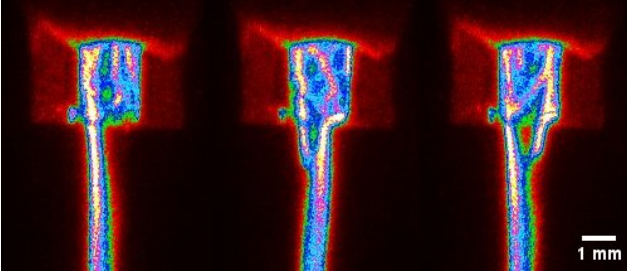


Figure 8: Fast-imaging of the first discharge at different pulses for 1000 sccm argon jet, no co-flow, 20 kHz, 200 ns pulses. Slides show one exposure of the first discharge in different pulses. The argon jet and the ionisation wave propagate from top to bottom. The surface-to-volume streamer passage occurs at different azimuth angles. Although these images provide only 2D projections of the IW trajectory, the thickness was measured to be  $380 \pm 87 \mu\text{m}$  at  $z = 0 \text{ mm}$  and  $793 \pm 12 \mu\text{m}$  at  $z = 4.5 \text{ mm}$ . The fast-imaging experimental setup is similar to previous works [22].

Furthermore, in N<sub>2</sub>-O<sub>2</sub> streamers, a lower concentration of oxygen has been associated with higher streamer branching probabilities [83, 84], possibly due to a lower rate of photoionisation, which could explain both the higher RSD and the broader profiles of the 100%N<sub>2</sub> case even away from the nozzle. Note that the 100%N<sub>2</sub> co-flow case can contain oxygen impurities ( $\leq 2 \text{ ppm}$ ) from the Ar and N<sub>2</sub> gas bottles so that photoionisation exists. Further downstream, the absorbance is usually more reproducible in the jet's centre, where the IW is more diffuse [22], and less so at the edges.

For the second discharge, further away from the nozzle, the peak absorbance is lower for 2%O<sub>2</sub> and 100%N<sub>2</sub> (0%O<sub>2</sub>) co-flow, see Figure 7, which translates to a lower Ar(1s<sub>5</sub>) density, see Figure 10. This could be related to a lower electronegative shielding and a less efficient focusing of the discharge into the jet axis [31], which is also evident from the spread of the RSD of the peak absorbance at 100%N<sub>2</sub>(0%O<sub>2</sub>), see Figure 9.

### 3.6 Ar(1s<sub>5</sub>) maximum density at different N<sub>2</sub>/O<sub>2</sub> co-flow gas fractions

Figure 10 shows the spatial profiles of the Ar(1s<sub>5</sub>) maximum density, measured with the TDLAS setup for the two discharges, and for different N<sub>2</sub>/O<sub>2</sub> co-flow gas fractions, including the Abel inversion of the left- and the right-hand sides of the transverse profiles. This was used to verify the cylindrical symmetry of the discharge, a necessary condition for the reliability of the Abel inversion. The non-symmetric regions correlate well with those of higher RSD; see Figure 9. The second discharge with a 100%N<sub>2</sub> co-flow showed no symmetric region. For both discharges, the spatial density profile funnels downstream. This is consistent with the

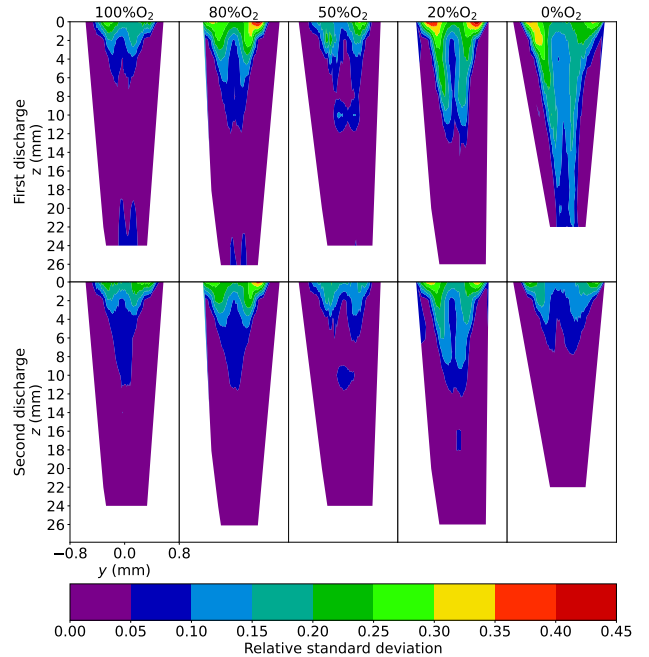


Figure 9: Relative standard deviation for the 1000 measures of peak absorbance, calculated at different  $(y, z)$  positions for the first discharge (first row) and the second discharge (second row), and different N<sub>2</sub>/O<sub>2</sub> co-flow gas fractions (depicted in the different columns).

progressive mixing of the shielding gas into the argon jet, favouring the quenching of Ar(1s<sub>5</sub>).

For 50% and 20% of O<sub>2</sub>, the profiles reach a narrow point at 14 mm, after which the profile broadens again. This behaviour is seen to a lesser degree at 16 mm for 80%O<sub>2</sub> co-flow. For 100%O<sub>2</sub> co-flow, there is no narrowing/broadening point for the profile of the maximum density. However, one observes the increase of the RSD after 20 mm; see Figure 9. We do not have a definite explanation for this peculiar shape. A possible reason is the off-axis trajectory of the IW at the end of its propagation path, as observed in fast imaging diagnostics, but further experiments should be conducted to properly analyze this effect.

In the symmetric region, the maximum density is always in the centre of the radial profile, where the higher Ar fraction region is also found. In all cases, the Ar(1s<sub>5</sub>) maximum density is of the order of  $10^{13} \text{ cm}^{-3}$ , with the highest value measured for 100%O<sub>2</sub>, and the lowest for 100%N<sub>2</sub>(0%O<sub>2</sub>), see Table 1.

Table 1: Maximum density of Ar(1s<sub>5</sub>) (units of  $[10^{13} \text{ cm}^{-3}]$ ) in the first and second discharges for different O<sub>2</sub> percentages in the shielding gas.

O <sub>2</sub> (%)	100%	80%	50%	20%	0%
1st discharge	9.1	7.3	7.1	8.9	5.8
2nd discharge	9.3	5.7	5.4	5.8	*

\*An Abel inversion could not be performed for this case.

The lower peak densities for 100%N<sub>2</sub> (0%O<sub>2</sub>) shielding could relate to a more filamentary discharge, again due to higher branching ratios [83, 84] and less repro-

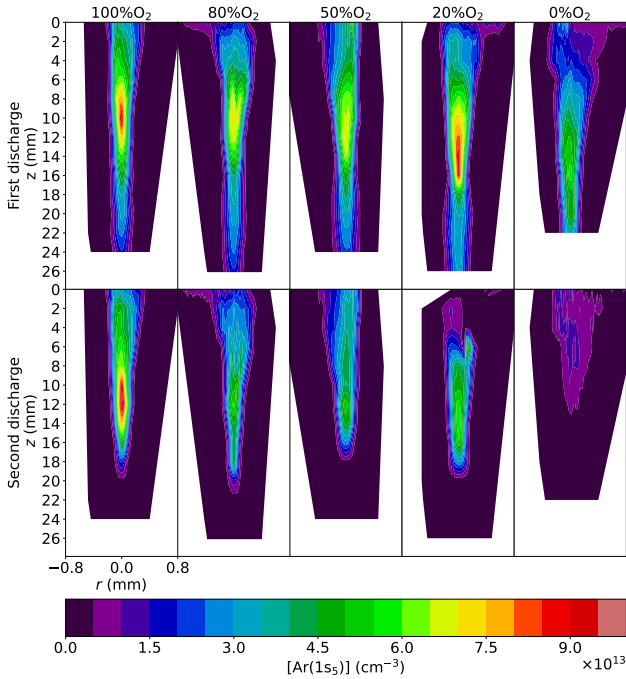


Figure 10: Spatial profiles of the maximum Ar(1s<sub>5</sub>) density at different ( $r, z$ ) positions, for the first discharge (first row) and the second discharge (second row), and different N<sub>2</sub>/O<sub>2</sub> co-flow gas fractions (depicted in the different columns). The negative/positive radial positions are as in Figure 6. The second discharge with a 100%N<sub>2</sub> (0%O<sub>2</sub>) co-flow showed no symmetric region.

ducible streamer trajectories. The overall higher RSD supports this possibility for the 100%N<sub>2</sub> shielding; see Figure 9. A more filamentary discharge would have a twofold effect of broadening the absorbance profile and lowering the median absorbance over 1000 pulses, decreasing the maximum value of the Ar(1s<sub>5</sub>) radial profile.

The high Ar(1s<sub>5</sub>) density for 20%O<sub>2</sub> shielding, see Table 1, cannot be explained by the previous hypothesis. One possibility is that this co-flow, with a relatively lower O<sub>2</sub> fraction, would mix less with argon (due to the lower viscosity of the nitrogen-dominated gas shielding [78, 79]) and the longer laminar length of a less turbulent flow. In this case, the quenching ratios would be lower (relative to higher O<sub>2</sub> fraction) [80] and the reproducibility higher than in the case of 100%N<sub>2</sub> (0%O<sub>2</sub>), see Figure 9. This combination of effects would explain the increase in the maximum Ar(1s<sub>5</sub>) density for 20%O<sub>2</sub> co-flows, but this hypothesis cannot explain the higher Ar(1s<sub>5</sub>) maximum density at 100%O<sub>2</sub> co-flows. It is possible that pure oxygen shielding presents more substantial memory effects, with anions functioning as electron reservoirs and limiting the diffusion loss of electrons between pulses, which would be coherent with the highest Ar(1s<sub>5</sub>) density on the secondary discharge, see Table 1 and Figure 10. Still, this suggests a missing mechanism involving N<sub>2</sub>, which cannot be explained with the current analysis.

The position of the maximum density shifts upstream from 14 mm to 10 mm with increasing O<sub>2</sub> fraction in the co-flow. This could be due to higher Ar/shielding-gas mixing, owing to the higher O<sub>2</sub> viscosity [79], which along with higher quenching rates for O<sub>2</sub> [80] would limit the maximum Ar(1s<sub>5</sub>) density position closer to the nozzle. The shift of the peak density position could also be associated with the decrease in laminar length; see section 3.3. Turbulence may increase the mixing between argon and the shielding gas. A shorter laminar length may lead to higher quenching rates closer to the nozzle, thus shifting the position of Ar(1s<sub>5</sub>) maximum density upstream.

Compared to the first discharge, the maximum density for the second discharge is lower for co-flow mixtures between 0% to 80%O<sub>2</sub>, see Table 1. The exception is 100%O<sub>2</sub>, where the maximum density is comparable for the two discharges. For the second discharge, the position of the maximum metastable density is always around 12 mm, whatever the co-flow mixture.

Unfortunately, the absorbance for 100%N<sub>2</sub>(0%O<sub>2</sub>) is too low and asymmetric, so the Abel inversion could not be performed. The low metastable density at 100%N<sub>2</sub> (0%O<sub>2</sub>) could be related to a higher plasma conductivity near the nozzle due to the lower anion density, leading to a shorter discharge propagation downstream along the axis.

The spatial density profiles also funnel downstream for the second discharge, see Figure 10, which is again consistent with the progressive mixing of the shielding gas into the argon jet, see Figure 5. The cone-like shape is more pronounced for 100% to 50% O<sub>2</sub> shieldings, approaching a cylindrical shape for 20% O<sub>2</sub> and below, possibly due to lower electronegative shielding. The position at which the spatial profile of the second discharge ends is near 20 mm, which for > 50%O<sub>2</sub> co-flows should be near the laminar to turbulent transition.

The high Ar(1s<sub>5</sub>) maximum density occurring during the second discharge at 100%O<sub>2</sub> co-flow is not easy to explain. The enhanced electronegative shielding for a pure O<sub>2</sub> co-flow may account for the higher density, but this does not explain the significant difference between the maximum density of the metastable for 100%O<sub>2</sub> and the other oxygenated shielding gas mixtures. This behaviour at 100%O<sub>2</sub> (0%N<sub>2</sub>) suggests a mechanism involving N<sub>2</sub>, which could not be identified in this analysis.

## 4 Conclusion

The argon  $\mu$ APPJs reactor studied in this work produces two discharges, one at the rising edge and the other at the falling edge of the applied voltage pulse. TDLAS allowed measuring Ar(1s<sub>5</sub>) absolute density radial profiles for each discharge. The first discharge is longer, broader, and less reproducible than the second discharge, generally leading to higher Ar(1s<sub>5</sub>) densities. In both discharges, the Ar(1s<sub>5</sub>) density profile funnels downstream, coherent with the shape of higher argon

molar fractions regions as found in the CFD simulation. The shielding gas significantly affects the Ar(1s<sub>5</sub>) density profiles. A dry-air co-flow increases the Ar(1s<sub>5</sub>) density compared with the ambient case. Since the argon jet flow is not significantly modified, this is possibly due to the lower H<sub>2</sub>O concentration. The absence of O<sub>2</sub> in the shielding gas leads to lower reproducibility and longer and broader Ar(1s<sub>5</sub>) density profiles. O<sub>2</sub> admixture significantly increases both discharges' reproducibility and Ar(1s<sub>5</sub>) density. The absence of N<sub>2</sub> leads to the highest Ar(1s<sub>5</sub>) density in both discharges.

Even with the complimentary Schlieren and CFD analysis, it isn't easy to quantify the interaction between plasma and flow dynamics. Furthermore, electrodynamic and chemical processes can vary significantly with different co-flow gas mixtures. Expanding this analysis may require a comprehensive Ar-N<sub>2</sub>-O<sub>2</sub> reactive scheme to be compared with detailed local and temporal Ar(1s<sub>5</sub>) density profiles. Even though our analysis is coherent with the current hypothesis on APPJ dynamics, it poses questions unanswered within the existing literature, such as how can the absence of N<sub>2</sub> in the shielding gas cause a significantly higher Ar(1s<sub>5</sub>) density in the second discharge compared with other shielding mixtures? This work also provides spatially accurate data of Ar(1s<sub>5</sub>) densities in limiting conditions, i.e. Ar-N<sub>2</sub> and Ar-O<sub>2</sub> gas mixtures, and details the behaviour in intermediate cases. This data is essential to plan future experimental studies and to validate numerical models. It may also aid in developing shielded argon  $\mu$ APPJs for different applications.

## 5 Acknowledgement

The authors thank Dr. Kristaq Gazeli (LSPM, CNRS) for the helpful discussions. The Portuguese FCT - Fundação para a Ciência e a Tecnologia, partially supported this work under projects UIDB/50010/2020, UIDP/50010/2020, LA/P/0061/2020, and grants PB/BD/142972/2018 and BL194/2022.

## References

- [1] M G Kong, B N Ganguly, and R F Hicks. Plasma jets and plasma bullets. *Plasma Sources Science and Technology*, 21(3):030201, jun 2012.
- [2] Thomas von Woedtke, Steffen Emmert, Hans-Robert Metelmann, Stefan Rupf, and Klaus-Dieter Weltmann. Perspectives on cold atmospheric plasma (CAP) applications in medicine. *Physics of Plasmas*, 27(7):070601, 07 2020.
- [3] Hiromasa Tanaka, Kenji Ishikawa, Masaaki Mizuno, Shinya Toyokuni, Hiroaki Kajiyama, Fumitaka Kikkawa, Hans-Robert Metelmann, and Masaru Hori. State of the art in medical applications using non-thermal atmospheric pressure plasma. *Reviews of Modern Plasma Physics*, 1(1):3, December 2017.
- [4] Kyriakos Sklias, João Santos Sousa, and Pierre-Marie Girard. Role of short- and long-lived reactive species on the selectivity and anti-cancer action of plasma treatment in vitro. *Cancers*, 13(4), 2021.
- [5] Sandra Martínez-Jarquín and Robert Winkler. Low-temperature plasma (ltp) jets for mass spectrometry (ms): Ion processes, instrumental setups, and application examples. *TrAC Trends in Analytical Chemistry*, 89:133–145, 2017.
- [6] K Gazeli, T Vazquez, G Bauville, N Blin-Simiand, B Bournonville, S Pasquiers, and J Santos Sousa. Experimental investigation of a ns-pulsed argon plasma jet for the fast desorption of weakly volatile organic compounds deposited on glass substrates at variable electric potential. *Journal of Physics D: Applied Physics*, 53(47):475202, sep 2020.
- [7] Damany, Xavier, Pasquiers, Stéphane, Blin-Simiand, Nicole, Bauville, Gérard, Bournonville, Blandine, Fleury, Michel, Jeanney, Pascal, and Sousa, João Santos. Impact of an atmospheric argon plasma jet on a dielectric surface and desorption of organic molecules\*. *Eur. Phys. J. Appl. Phys.*, 75(2):24713, 2016.
- [8] J. Benedikt, K. Focke, A. Yanguas-Gil, and A. von Keudell. Atmospheric pressure microplasma jet as a depositing tool. *Applied Physics Letters*, 89(25):251504, 12 2006.
- [9] Alonso H. Ricci Castro, Felipe V.P. Kodaira, Vadym Prysiashnyi, Rogerio P. Mota, and Konstantin G. Kostov. Deposition of thin films using argon/acetylene atmospheric pressure plasma jet. *Surface and Coatings Technology*, 312:13–18, 2017. 13th International Conference on Plasma-Based Ion Implantation and Deposition.
- [10] Oleksiy V. Penkov, Mahdi Khadem, Won-Suk Lim, and Dae-Eun Kim. A review of recent applications of atmospheric pressure plasma jets for materials processing. *Journal of Coatings Technology and Research*, 12(2):225–235, March 2015.
- [11] J Winter, R Brandenburg, and K-D Weltmann. Atmospheric pressure plasma jets: an overview of devices and new directions. *Plasma Sources Science and Technology*, 24(6):064001, oct 2015.
- [12] Sander Nijdam, Jannis Teunissen, and Ute Ebert. The physics of streamer discharge phenomena. *Plasma Sources Science and Technology*, 29(10):103001, oct 2020.
- [13] XinPei Lu and Kostya (Ken) Ostrikov. Guided ionization waves: The physics of repeatability. *Applied Physics Reviews*, 5(3):031102, 07 2018.
- [14] K. Gazeli, P. Svarnas, P. Vafeas, P. K. Papadopoulos, A. Gkelios, and F. Clément. Investigation on streamers propagating into a helium jet

- in air at atmospheric pressure: Electrical and optical emission analysis. *Journal of Applied Physics*, 114(10):103304, 09 2013.
- [15] J. L. Walsh, J. J. Shi, and M. G. Kong. Contrasting characteristics of pulsed and sinusoidal cold atmospheric plasma jets. *Applied Physics Letters*, 88(17):171501, 04 2006.
- [16] Keiichiro Urabe, Tadasuke Morita, Kunihide Tachibana, and Biswa N Ganguly. Investigation of discharge mechanisms in helium plasma jet at atmospheric pressure by laser spectroscopic measurements. *Journal of Physics D: Applied Physics*, 43(9):095201, feb 2010.
- [17] Q. Th. Algwari and D. O’Connell. Electron dynamics and plasma jet formation in a helium atmospheric pressure dielectric barrier discharge jet. *Applied Physics Letters*, 99(12):121501, 09 2011.
- [18] Asma Begum, Mounir Laroussi, and Mohammad Rasel Pervez. Atmospheric pressure He-air plasma jet: Breakdown process and propagation phenomenon. *AIP Advances*, 3(6):062117, 06 2013.
- [19] A Sobota, O Guaitella, and A Rousseau. The influence of the geometry and electrical characteristics on the formation of the atmospheric pressure plasma jet. *Plasma Sources Science and Technology*, 23(2):025016, mar 2014.
- [20] S Hübner, J Santos Sousa, V Puech, G M W Kroesen, and N Sadeghi. Electron properties in an atmospheric helium plasma jet determined by thomson scattering. *Journal of Physics D: Applied Physics*, 47(43):432001, oct 2014.
- [21] J Winter, J Santos Sousa, N Sadeghi, A Schmidt-Bleker, S Reuter, and V Puech. The spatio-temporal distribution of he (23s1) metastable atoms in a mhz-driven helium plasma jet is influenced by the oxygen/nitrogen ratio of the surrounding atmosphere. *Plasma Sources Science and Technology*, 24(2):025015, mar 2015.
- [22] Et. Es-sebbar, G. Bauville, M. Fleury, S. Pasquiers, and J. Santos Sousa. Spatio-temporal distribution of absolute densities of argon metastable 1s5 state in the diffuse area of an atmospheric pressure nanosecond pulsed argon microplasma jet propagating into ambient air. *Journal of Applied Physics*, 126(7):073302, 08 2019.
- [23] Kristaq Gazeli, Thomas Vazquez, Sara Al-Homsi, Gérard Bauville, Nicole Blin-Simiand, Blandine Bournonville, Michel Fleury, Pascal Jeanney, Olivier Neveu, Stéphane Pasquiers, and João Santos Sousa. Ar(1s5) absolute radial densities in a ns-pulsed argon plasma jet impinging on dielectric targets at floating potential – plasma action on organic molecules. *Plasma Processes and Polymers*, 15(10):1800080, 2018.
- [24] K Gazeli, G Bauville, M Fleury, P Jeanney, O Neveu, S Pasquiers, and J Santos Sousa. Effect of the gas flow rate on the spatiotemporal distribution of ar(1s5) absolute densities in a ns pulsed plasma jet impinging on a glass surface. *Plasma Sources Science and Technology*, 27(6):065003, jun 2018.
- [25] Hideki Motomura, Hisaki Matsuba, Masanori Kawata, and Masafumi Jinno. Gas-specific characteristics of argon low-frequency atmospheric-pressure nonequilibrium microplasma jet. *Japanese Journal of Applied Physics*, 46(10L):L939, sep 2007.
- [26] R Bussiahn, E Kindel, H Lange, and K-D Weltmann. Spatially and temporally resolved measurements of argon metastable atoms in the effluent of a cold atmospheric pressure plasma jet. *Journal of Physics D: Applied Physics*, 43(16):165201, apr 2010.
- [27] Hyun Kim, Albrecht Brockhaus, and Jürgen Engemann. Atmospheric pressure argon plasma jet using a cylindrical piezoelectric transformer. *Applied Physics Letters*, 95(21):211501, 11 2009.
- [28] K Gazeli, T Vazquez, G Bauville, N Blin-Simiand, B Bournonville, S Pasquiers, and J Santos Sousa. Experimental investigation of a ns-pulsed argon plasma jet for the fast desorption of weakly volatile organic compounds deposited on glass substrates at variable electric potential. *Journal of Physics D: Applied Physics*, 53(47):475202, sep 2020.
- [29] Qing Li, Wen-Chao Zhu, Xi-Ming Zhu, and Yi-Kang Pu. Effects of penning ionization on the discharge patterns of atmospheric pressure plasma jets. *Journal of Physics D: Applied Physics*, 43(38):382001, sep 2010.
- [30] X. Lu, G.V. Naidis, M. Laroussi, and K. Ostrikov. Guided ionization waves: Theory and experiments. *Physics Reports*, 540(3):123–166, 2014. Guided ionization waves: Theory and experiments.
- [31] Ansgar Schmidt-Bleker, Seth A Norberg, Jörn Winter, Eric Johnsen, S Reuter, K D Weltmann, and Mark J Kushner. Propagation mechanisms of guided streamers in plasma jets: the influence of electronegativity of the surrounding gas. *Plasma Sources Science and Technology*, 24(3):035022, jun 2015.
- [32] XinPei Lu, DaWei Liu, YuBin Xian, LanLan Nie, YingGuang Cao, and GuangYuan He. Cold atmospheric-pressure air plasma jet: Physics and opportunities. *Physics of Plasmas*, 28(10):100501, 10 2021.
- [33] Pedro Viegas, Elmar Slikboer, Zdenek Bonaventura, Olivier Guaitella, Ana Sobota, and Anne

- Bourdon. Physics of plasma jets and interaction with surfaces: review on modelling and experiments. *Plasma Sources Science and Technology*, 31(5):053001, may 2022.
- [34] S Iseni, A Schmidt-Bleker, J Winter, K-D Weltmann, and S Reuter. Atmospheric pressure streamer follows the turbulent argon air boundary in a mhz argon plasma jet investigated by oh-tracer plif spectroscopy. *Journal of Physics D: Applied Physics*, 47(15):152001, mar 2014.
- [35] Youssef Morabit, Richard D. Whalley, Eric Robert, Mohammad I. Hasan, and James L. Walsh. Turbulence and entrainment in an atmospheric pressure dielectric barrier plasma jet. *Plasma Processes and Polymers*, 17(6):1900217, 2020.
- [36] I L Semenov and K-D Weltmann. Modelling of turbulent reacting flow for a cold atmospheric pressure argon plasma jet. *Plasma Sources Science and Technology*, 29(5):055001, apr 2020.
- [37] Thibault Darny, Gérard Bauville, Michel Fleury, Stéphane Pasquiers, and João Santos Sousa. Periodic forced flow in a nanosecond pulsed cold atmospheric pressure argon plasma jet. *Plasma Sources Science and Technology*, 30(10):105021, oct 2021.
- [38] Amanda M. Lietz, Eric Johnsen, and Mark J. Kushner. Plasma-induced flow instabilities in atmospheric pressure plasma jets. *Applied Physics Letters*, 111(11):114101, 09 2017.
- [39] René van Hout, Sudharson Murugan, Abhijit Mitra, and Beni Cukurel. Coaxial circular jets—a review. *Fluids*, 6(4), 2021.
- [40] Stephan Reuter, Jörn Winter, Ansgar Schmidt-Bleker, Helena Tresp, Malte U. Hammer, and Klaus-Dieter Weltmann. Controlling the ambient air affected reactive species composition in the effluent of an argon plasma jet. *IEEE Transactions on Plasma Science*, 40(11):2788–2794, 2012.
- [41] A Schmidt-Bleker, J Winter, S Iseni, M Dünnbier, K-D Weltmann, and S Reuter. Reactive species output of a plasma jet with a shielding gas device—combination of ftir absorption spectroscopy and gas phase modelling. *Journal of Physics D: Applied Physics*, 47(14):145201, mar 2014.
- [42] Yubin Xian, Xinpei Lu, Yinguang Cao, Ping Yang, Qing Xiong, Zhonghe Jiang, and Yuan Pan. On plasma bullet behavior. *IEEE Transactions on Plasma Science*, 37(10):2068–2073, 2009.
- [43] S. Wu, X. Lu, and Y. Pan. Effects of seed electrons on the plasma bullet propagation. *Current Applied Physics*, 13:S1–S5, 2013. Special Issue: SPB 2012.
- [44] T. Y. Tang, H. S. Kim, G. H. Kim, B. Lee, and H. J. Lee. Optical diagnostics of the characteristics of a square unipolar nanosecond pulse-driven atmospheric pressure helium plasma jet. *AIP Advances*, 10(12):125218, 12 2020.
- [45] Song Jiang, Guojie Shi, Yonggang Wang, Zi Li, Junfeng Rao, and Zhonghang Wu. Discharge characteristics of atmospheric pressure ar/n<sub>2</sub>/o<sub>2</sub> plasma jet under a square wave pulse. *IEEE Transactions on Plasma Science*, 50(10):3652–3658, October 2022.
- [46] J L Walsh, F Iza, N B Janson, V J Law, and M G Kong. Three distinct modes in a cold atmospheric pressure plasma jet. *Journal of Physics D: Applied Physics*, 43(7):075201, feb 2010.
- [47] B Niermann, R Reuter, T Kuschel, J Benedikt, M Böke, and J Winter. Argon metastable dynamics in a filamentary jet micro-discharge at atmospheric pressure. *Plasma Sources Science and Technology*, 21(3):034002, apr 2012.
- [48] Muyang Qian, Chunsheng Ren, Dezhen Wang, Jialiang Zhang, and Guodong Wei. Stark broadening measurement of the electron density in an atmospheric pressure argon plasma jet with double-power electrodes. *Journal of Applied Physics*, 107(6):063303, 03 2010.
- [49] Jan Schäfer, Florian Sigener, Rüdiger Foest, Detlef Loffhagen, and Klaus-Dieter Weltmann. On plasma parameters of a self-organized plasma jet at atmospheric pressure. *The European Physical Journal D*, 60:531, 12 2010.
- [50] S Hofmann, A F H van Gessel, T Verreycken, and P Bruggeman. Power dissipation, gas temperatures and electron densities of cold atmospheric pressure helium and argon rf plasma jets. *Plasma Sources Science and Technology*, 20(6):065010, nov 2011.
- [51] F. Judée, N. Merbahi, G. Wattieaux, and M. Yousfi. Analysis of Ar plasma jets induced by single and double dielectric barrier discharges at atmospheric pressure. *Journal of Applied Physics*, 120(11):114901, September 2016.
- [52] Elmar Slikboer and James L Walsh. Characterization of a khz sinusoidal argon plasma jet impinging on water using thomson scattering and fast imaging. *Journal of Physics D: Applied Physics*, 54(32):325201, jun 2021.
- [53] Elmar Slikboer and James Walsh. Impact of electrical grounding conditions on plasma–liquid interactions using thomson scattering on a pulsed argon jet. *Scientific Reports*, 11(1):17749, September 2021.
- [54] Joao Santos Sousa, S. Hübner, Ana Sobota, Stéphane Pasquiers, Vincent Puech, and Nader

- Sadeghi. Electron properties in atmospheric pressure plasma jets determined by Thomson scattering. *Proceedings of the 23rd ESCAMPIG, Bratislava, Slovakia*, 23, July 2016.
- [55] Rok Zaplotnik, Marijan Bišćan, Nikša Krstulović, Dean Popović, and Slobodan Milošević. Cavity ring-down spectroscopy for atmospheric pressure plasma jet analysis. *Plasma Sources Science and Technology*, 24(5):054004, aug 2015.
- [56] Stephan Reuter, Joao Santos Sousa, Gabi Daniel Stancu, and Jean-Pierre Hubertus van Helden. Review on vuv to mir absorption spectroscopy of atmospheric pressure plasma jets. *Plasma Sources Science and Technology*, 24(5):054001, aug 2015.
- [57] Brian L Sands, Robert J Leiweke, and Biswa N Ganguly. Spatiotemporally resolved ar (1s5) metastable measurements in a streamer-like he/ar atmospheric pressure plasma jet. *Journal of Physics D: Applied Physics*, 43(28):282001, jun 2010.
- [58] Sandra Schröter, Ramasamy Pothiraja, Peter Awakowicz, Nikita Bibinov, Marc Böke, Benedikt Niermann, and Jörg Winter. Time-resolved characterization of a filamentary argon discharge at atmospheric pressure in a capillary using emission and absorption spectroscopy. *Journal of Physics D: Applied Physics*, 46(46):464009, oct 2013.
- [59] Ansgar Schmidt-Bleker, Jörn Winter, André Bösel, Stephan Reuter, and Klaus-Dieter Weltmann. On the plasma chemistry of a cold atmospheric argon plasma jet with shielding gas device. *Plasma Sources Science and Technology*, 25(1):015005, dec 2015.
- [60] Claire Douat, Issaad Kacem, Nader Sadeghi, Gérard Bauville, Michel Fleury, and Vincent Puech. Space-time resolved density of helium metastable atoms in a nanosecond pulsed plasma jet: influence of high voltage and pulse frequency. *Journal of Physics D: Applied Physics*, 49(28):285204, jun 2016.
- [61] Nader Sadeghi. Practical aspects of molecular spectroscopy in plasmas 6. molecular spectroscopy techniques applied for processing plasma diagnostics. *Journal of Plasma and Fusion Research*, 80(9):767–776, 2004.
- [62] Eric W. Weisstein. “Lorentzian Function”. From MathWorld – A Wolfram Web Resource. [mathworld.wolfram.com/lorentzianfunction.html](http://mathworld.wolfram.com/lorentzianfunction.html). Last visited on 23/2/2024.
- [63] Hans R. Griem. *Principles of Plasma Spectroscopy*. Cambridge University Press, 2005.
- [64] C O Laux, T G Spence, C H Kruger, and R N Zare. Optical diagnostics of atmospheric pressure air plasmas. *Plasma Sources Science and Technology*, 12(2):125, feb 2003.
- [65] W. L. Wiese, J. W. Brault, K. Danzmann, V. Helbig, and M. Kock. Unified set of atomic transition probabilities for neutral argon. *Phys. Rev. A*, 39:2461–2471, Mar 1989.
- [66] Wolfgang Demtröder. *Laser Spectroscopy*. Springer, Berlin, 1996.
- [67] Hans R. Griem. *Spectral line broadening by plasmas*. Academic Press, 1974.
- [68] R. Konjević and N. Konjević. On the use of non-hydrogenic spectral line profiles for electron density diagnostics of inductively coupled plasmas. *Spectrochimica Acta Part B: Atomic Spectroscopy*, 52(14):2077–2084, 1997.
- [69] Terry N. Olney, N.M. Cann, Glyn Cooper, and C.E. Brion. Absolute scale determination for photoabsorption spectra and the calculation of molecular properties using dipole sum-rules. *Chemical Physics*, 223(1):59–98, 1997.
- [70] Daniel D. Hickstein, Stephen T. Gibson, Roman Yurchak, Dhruvajyoti D. Das, and Mikhail Ryazanov. A direct comparison of high-speed methods for the numerical Abel transform, 06 2019.
- [71] Israel Beniaminy and Moshe Deutsch. Abel: Stable, high accuracy program for the inversion of abel’s integral equation. *Computer Physics Communications*, 27(4):415–422, 1982.
- [72] Bruno Lopez and Mario Lino Da Silva. Spark: A software package for aerodynamics, radiation and kinetics. *46th AIAA Thermophysics Conference*, 2016.
- [73] E. Turkel. Preconditioning techniques in computational fluid dynamics. *Annual Review of Fluid Mechanics*, 31(1):385–416, 1999.
- [74] Eiji Shima and Keiichi Kitamura. Parameter-free simple low-dissipation ausm-family scheme for all speeds. *AIAA Journal*, 49(8):1693–1709, 2011.
- [75] Xu-Dong Liu, Stanley Osher, and Tony Chan. Weighted essentially non-oscillatory schemes. *Journal of Computational Physics*, 115(1):200–212, 1994.
- [76] Daniel Dias Loureiro. High-temperature modeling of transport properties in hypersonic flows. Master’s thesis, University of Lisbon, Instituto Superior Técnico, 2015. Issue: November.
- [77] Roger A Svehla. Estimated viscosities and thermal conductivities of gases at high temperatures. Technical Report NASA-TR-R-132, NASA, Langley Research Center, Hampton VA 23681-2199, USA, January 1962.
- [78] Kenneth K. Kuo. *Principles of combustion*. John Wiley, Hoboken, NJ, 2nd ed edition, 2005.

- [79] E.W. Lemmon and R.T Jacobsen. Viscosity and thermal conductivity equations for nitrogen, oxygen, argon, and air. *International Journal of Thermophysics*, 25:21–69, 01 2004.
- [80] L. G. Piper, J. E. Velazco, and D. W. Setser. Quenching cross sections for electronic energy transfer reactions between metastable argon atoms and noble gases and small molecules. *The Journal of Chemical Physics*, 59(6):3323–3340, 09 2003.
- [81] N L Aleksandrov and E M Bazelyan. Ionization processes in spark discharge plasmas. *Plasma Sources Science and Technology*, 8(2):285, may 1999.
- [82] Alejandro Malagón-Romero and Alejandro Luque. Streamer propagation in humid air. *Plasma Sources Science and Technology*, 31(10):105010, oct 2022.
- [83] She Chen, Feng Wang, Qiuqin Sun, and Rong Zeng. Branching characteristics of positive streamers in nitrogen-oxygen gas mixtures. *IEEE Transactions on Dielectrics and Electrical Insulation*, 25(3):1128–1134, 2018.
- [84] S Nijdam, F M J H van de Wetering, R Blanc, E M van Veldhuizen, and U Ebert. Probing photoionization: experiments on positive streamers in pure gases and mixtures. *Journal of Physics D: Applied Physics*, 43(14):145204, mar 2010.